Manipulation of saturation magnetization and perpendicular magnetic anisotropy in epitaxial $Co_xMn_{4-x}N$ films with ferrimagnetic compensation

Keita Ito[1,*], Yoko Yasutomi,[1] Siyuan Zhu,[2] Munisa Nurmamat[2], Masaki Tahara,[3] Kaoru Toko,[1] Ryota Akiyama[4],
Yukiharu Takeda,[5] Yuji Saitoh,[5] Tamio Oguchi,[3] Akio Kimura,[2] and Takashi Suemasu[1]

[1]*Institute of Applied Physics, University of Tsukuba, Tsukuba, Ibaraki 305–8573, Japan*
[2]*Graduate School of Science, Hiroshima University, Higashi-Hiroshima, Hiroshima 739–8526, Japan*
[3]*The Institute of Scientific and Industrial Research, Osaka University, Ibaraki, Osaka 567–0047, Japan*
[4]*Department of Physics, The University of Tokyo, Bunkyo-ku, Tokyo 113–0033, Japan*
[5]*Materials Sciences Research Center, Japan Atomic Energy Agency, Sayo, Hyogo 679–5148, Japan*

Spintronics devices utilizing a magnetic domain-wall motion have attracted increasing attention, and ferrimagnetic materials with almost-compensated magnetic moments are highly required to realize the fast magnetic domain-wall motion. Here, we report a key function for this purpose in the antiperovskite $Co_xMn_{4-x}N$ film. We have grown $Co_xMn_{4-x}N$ films with various Co/Mn ratios on $SrTiO_3(001)$ by molecular-beam epitaxy. High-quality growth is confirmed and a perpendicular magnetization emerges at $x = 0, 0.2, 0.5$, and 0.8, whereas it turns into in plane for $x \geqslant 1.1$. The saturation magnetization M_S decreases as x increases and reaches a minimum value of $15\,\mathrm{emu/cm^3}$ at $x = 0.8$. Then, it increases with x when $0.8 \leqslant x \leqslant 3.6$ and saturates. These results indicate that M_S and magnetic anisotropy of $Co_xMn_{4-x}N$ films can be manipulated by the Co composition. X-ray absorption spectroscopy and magnetic circular dichroism measurements revealed that Co atoms tend to occupy the I site in the antiperovskite lattice and reasonably explains the origin of minimum M_S near $x = 0.8$, where a compensation of magnetic moments occurs among different atomic sites. We consider that the nearly compensated ferrimagnetic $Co_{0.8}Mn_{3.2}N$ is suitable for application to current-induced domain-wall motion devices.

I. INTRODUCTION

Spintronics has gained much attention as an emerging research topic of targeting novel functional devices utilizing both electron's charge and spin. For instance, a spin-transfer torque-driven magnetic random access memory [1] and a current-induced magnetic domain-wall motion device [2] were proposed. Ferromagnetic films possessing perpendicular magnetic anisotropy (PMA) are required to improve the performance of these spintronics devices [3–7]. The perpendicular magnetization was reported in antiperovskite nitride Mn_4N films grown on various substrates such as glass [8], Si(001) [9], MgO(001) [10–13], and $SrTiO_3(STO)(001)$ [11]. Figure 1 shows a schematic of the antiperovskite lattice. Mn_4N is a cubic ferrimagnetic metal with the Curie temperature of 745 K, and the lattice constant of bulk samples is 0.3865 nm [14]. One N atom is located at the body center of the cube and the Mn atoms are at the corner (I) and face-centered (II) sites. The spin magnetic moments per Mn atom in Mn_4N were determined to be $m_{\mathrm{spin}}[\mathrm{Mn(I)}] = 3.85\mu_B$ and $m_{\mathrm{spin}}[\mathrm{Mn(IIA) and Mn(IIB)}] = -0.90\mu_B$ for a saturation magnetization of $1.14\mu_B$/formula units (f.u.) at 77 K from a neutron-diffraction measurement [14]. Here, μ_B is the Bohr

magneton. The magnetic and transport properties of epitaxial Mn_4N films grown on MgO(001) by pulsed laser deposition have been investigated, and a relatively large anomalous Hall effect is observed [12]. In addition, fast current-induced magnetic domain-wall motion owing to spin-transfer torque is reported [15], paving the way to sustainable spintronics devices. We have succeeded in growing 15–30-nm-thick epitaxial Mn_4N films on MgO(001) and STO(001) substrates by molecular-beam epitaxy (MBE) [11], and observed PMA. Our x-ray diffraction (XRD) measurement confirmed the tetragonal lattice formation with a ratio of the out-of-plane lattice constant c to the in-plane lattice constant $a,c/a$ of 0.99, which could be considered as an origin of PMA [11]. It was reported in Refs. [10], [12], and [13] that this c/a ratio was independent of the film thickness and substrates used. We have also paid special attention to other antiperovskite ferromagnetic nitrides such as Fe_4N and Co_4N, and their alloys ($Co_xFe_{4-x}N$), which are predicted to have a large negative spin polarization in the density of states at the Fermi level (Co_4N and Co_3FeN) or in electrical conductivity (Fe_4N) [16–18]. Ternary alloys consisting of antiperovskite magnetic nitrides attract much attention in terms of the growing flexibility in controlling their electronic structures and magnetic properties via the compositional variation of the 3d elements. In fact, synthesis and characterization of numerous antiperovskite-based nitrides such as $Ni_xMn_{4-x}N$, $Fe_xMn_{4-x}N$, and $Ni_xFe_{4-x}N$ have been carried out from the viewpoints of both theories

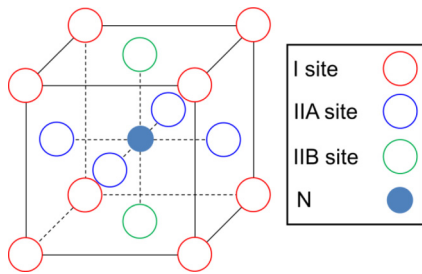*Present address: Institute for Materials Research, Tohoku University, Sendai 980-8577, Japan; itok@imr.tohoku.ac.jp

FIG. 1. Schematic of an antiperovskite-type lattice structure.

and experiments [19–27]. We achieved epitaxial growth of $Co_xFe_{4-x}N$ films on STO(001) substrates [28–30]. Element-specific magnetic moments, electronic structures, and transport properties of the $Co_xFe_{4-x}N$ films were studied by x-ray magnetic circular dichroism (XMCD) in x-ray absorption spectroscopy (XAS) [31–33], spin-resolved photoemission spectroscopy [34], and anisotropic magnetoresistance [35]. The atomic disorders of Co-Fe in the antiperovskite lattice and the sign of spin polarization were revealed. In contrast, there have been no reports thus far on the growth of $Co_xMn_{4-x}N$ films, and thereby their fundamental properties have yet to be investigated. Recently, magnetic compensation in $Ni_xMn_{4-x}N$ is reported at composition between $x = 0.1$ and 0.25 [20]. We also imagine that the addition of Co atoms into Mn_4N might cause the ferrimagnetic compensation, and it is a desirable feature for magnetic domain-wall motion devices.

In this study, we grew epitaxial $Co_xMn_{4-x}N$ films with x ranging from 0 to 4 on STO(001) substrates by MBE, and evaluated their c/a, saturation magnetization (M_S), magnetic anisotropy, and element-specific magnetic properties. Through these experiments, we discuss the crystalline qualities and magnetic properties of the $Co_xMn_{4-x}N$ films.

II. EXPERIMENTS AND CALCULATION

Approximately 10-nm-thick MBE-grown $Co_xMn_{4-x}N$ films were prepared on STO(001) substrates with x varied as 0, 0.2, 0.5, 0.8, 1.1, 1.3, 1.7, 2.3, 2.8, 3.6, and 4.0. The lattice mismatches to STO ($a = 0.3905$ nm) are -1.0% for Mn_4N ($a = 0.3865$ nm in Ref. [14]) and -8.2% for Co_4N ($a = 0.3586$ nm in Ref. [36]). The $Co_xMn_{4-x}N$ layers were grown at 450 °C by supplying Co and Mn molecular beams and radio-frequency N_2 plasma simultaneously. x can be controlled by changing the temperature of the crucibles in Knudsen cells for solid Co and Mn sources. After the growth of the nitride layers, an Al or Au capping layer was formed *in situ* to prevent oxidation of the nitrides. Rutherford backscattering spectrometry and electron probe microanalyzer measurements were performed to evaluate x. The crystalline quality of the samples was characterized by XRD measurements with a Cu $K\alpha$ radiation source and reflection high-energy electron diffraction (RHEED) observed along the STO[100] azimuth. Lattice constants, a and c, and the ratio c/a of the $Co_xMn_{4-x}N$ layers were deduced from out-of-plane (ω-2θ) and in-plane (ϕ-$2\theta\chi$) XRD measurements, or x-ray reciprocal lattice mapping. Magnetization versus magnetic field (M-H) curves were measured at 300 K using a superconducting quantum inter-

ference device magnetometer. External magnetic fields (H) of -50 to 50 kOe were applied parallel or perpendicular to the film surface. To determine the volumes of the $Co_xMn_{4-x}N$ layers for calculating their M_S value per unit volume, the layer thicknesses were deduced with the x-ray reflectometry method and the areas were estimated by using top-view photos of the samples. For the Mn_4N, $Co_{0.8}Mn_{3.2}N$, and Co_4N [32] films, we performed XAS and XMCD spectroscopies at 300 K for the Co and/or Mn $L_{2,3}$ edges using the total electron yield method at the twin helical undulator beamline BL23SU [37] of SPring-8 in Japan. With this, element-specific magnetic properties of Co and Mn atoms in the $Co_{0.8}Mn_{3.2}N$ film were investigated. Circularly polarized soft x rays were incident along positive or negative H (80 kOe for Mn_4N and 30 kOe for $Co_{0.8}Mn_{3.2}N$) applied perpendicular to the film surface during the measurements, and we used their averaged spectra for analysis.

XAS and XMCD spectra at the Mn $L_{2,3}$ edges of Mn_4N were simulated by a combination of a first-principles calculation using the all-electron full-potential linearized augmented-plane-wave (FLAPW) method and Fermi's golden rule with E1 transitions. Self-consistent-field calculations were performed with the scalar relativistic scheme plus the spin-orbit coupling in the second variation at every iteration. Some more details of the methods were described in a previous paper [38].

III. RESULTS AND DISCUSSION

A. Characterizations of crystalline quality and lattice constants

Figures 2(a)–2(f) display the ω-2θ XRD and RHEED patterns of the $Co_xMn_{4-x}N$ films ($x = 0$, 0.8, 1.1, 2.3, 2.8, and 4.0). The diffraction lines corresponding to (001)-oriented $Co_xMn_{4-x}N$ are observed except for $x = 1.1$. As for $x = 2.3$ and 2.8, only small 002 lines can be found as indicated by the black arrows in Figs. 2(d) and 2(e). The absence of additional peaks in the XRD data indicates that no secondary phases are detected in all the films. The RHEED patterns show streaks in all the $Co_xMn_{4-x}N$ layers, signifying the formation of epitaxial $Co_xMn_{4-x}N$ films. However, the streaks become diffusive for x departing from 0 and 4, and the half-order streaks shown by the white arrows in Figs. 2(a) and 2(f), which correspond to the superlattice diffractions related to the long-range atomic order of the N atoms, are not observed. These results show that the crystallinity of the $Co_xMn_{4-x}N$ films is slightly degraded.

Figure 3 shows the in-plane lattice constant a, out-of-plane lattice constant c, and c/a as a function of x deduced from the ω-2θ and ϕ-$2\theta\chi$ XRD measurements, or x-ray reciprocal lattice mapping for the $Co_xMn_{4-x}N$ ($x = 0$, 0.2, 0.5, 0.8, 2.8, 3.6, and 4.0) films. In the Mn-rich films ($0 \leqslant x \leqslant 0.8$), the lattice constants a and c are very close to the cubic lattice constant of Mn_4N (0.3865 nm) [14], and show no significant variation. In the Co-rich samples ($x \geqslant 2.8$), the lattice constant of the $Co_xMn_{4-x}N$ films gradually decreases with increasing x. These values are close to a reported value of Co_4N films (0.3586 nm) [36]. The tetragonally distorted lattice ($c/a = 0.98 - 0.99$) is maintained for all the $Co_xMn_{4-x}N$ films.

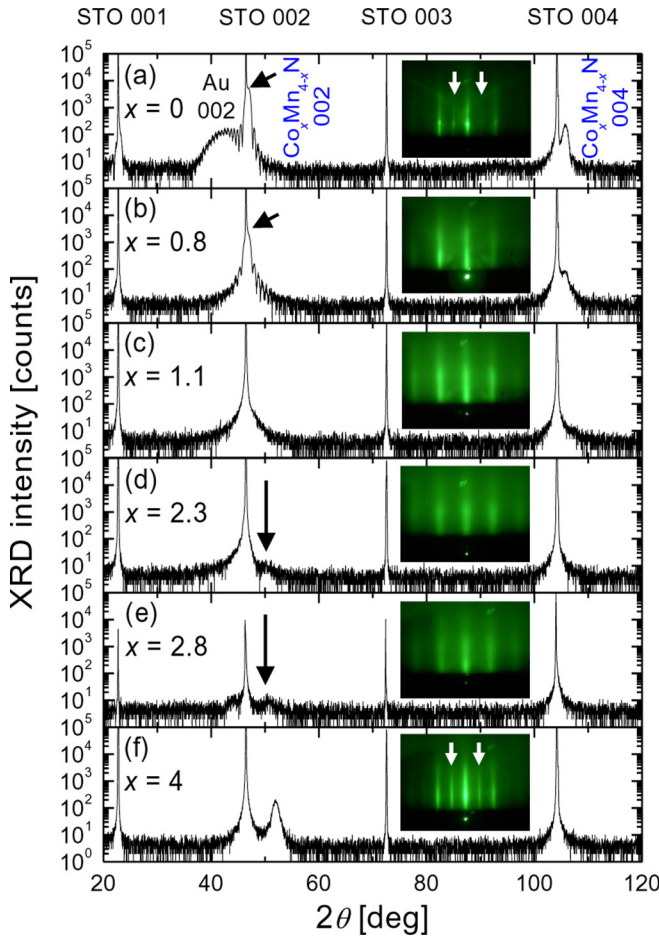FIG. 2. ω-2θ XRD patterns of the $Co_xMn_{4-x}N$ films ($x = 0$, 0.8, 1.1, 2.3, 2.8, and 4.0) on STO(001) substrates. Arrows in (d) and (e) are a guide to indicate the peak position of 002. The insets show the RHEED patterns of the nitride layers taken along STO[100] direction.

B. Magnetic properties

Figures 4(a)–4(d) show the M-H curves of the $Co_xMn_{4-x}N$ films ($x = 0.8$, 1.1, 2.3, and 2.8). As to $x = 0.8$ [Fig. 4(a)], the hysteresis curve is open and closed for out-of-plane and in-plane H, respectively. Similar features are also observed for samples with $x = 0$ [11,39], 0.2, and 0.5, demonstrating the perpendicular magnetization up to $x = 0.8$ of the $Co_xMn_{4-x}N$ films [10–13]. On the other hand, the values of the remanent magnetization (M_r) of the $Co_xMn_{4-x}N$ films with $x \geqslant 1.1$ [Figs. 4(b)–4(d)] under in-plane H are larger than those for out-of-plane H, indicating that the magnetization easy axis changes to the in-plane direction for $x \geqslant 1.1$. The coercive force of the perpendicular M-H curves (blue lines in Fig. 4) also becomes small for $x \geqslant 1.1$. The perpendicular magnetization is a distinctive characteristic of the Mn_4N films [10–13] among the binary alloy antiperovskite nitrides. In contrast, Co_4N films on STO show an in-plane magnetization [29]. For $x = 0.8$, M_S is 15 emu/cm³ and the anisotropy field (H_k) is approximately 30 kOe. The uniaxial magnetic anisotropy energy $K_u \approx M_S H_k/2$ is thus estimated to be 2.3×10^5 erg/cm³. The reported K_u values for Mn_4N films grown on MgO(001) by MBE [11] and sputtering [13] are 2.2×10^6 and
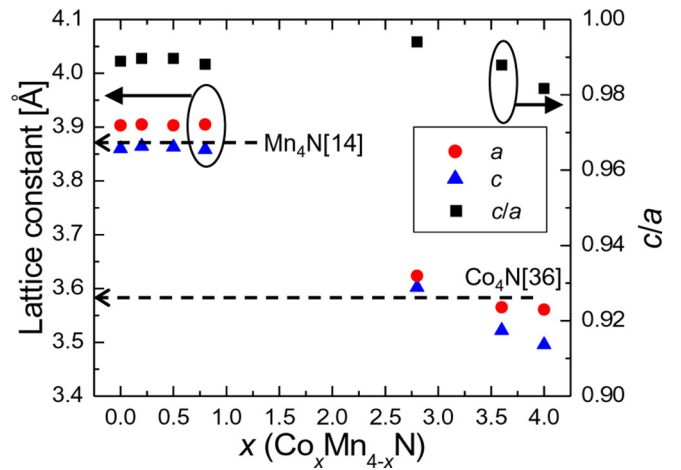

FIG. 3. In-plane and perpendicular-to-plane lattice constants (a and c), and c/a of the $Co_xMn_{4-x}N$ films. Broken lines show the reported lattice constants of Mn_4N and Co_4N.

8.8×10^5 erg/cm³, respectively. The addition of a small amount of Co into Mn_4N decreases K_u. In the vicinity of $x = 0.8$, the easy magnetization axis switches from the out-of-plane to in-plane direction of the film. It means that the in-plane component is included and the squareness (M_r/M_S) of the perpendicular magnetization curve is lowered when $x = 0.8$. This is natural and is unlikely to be due to the segregation of atoms.

Figure 4(e) presents M_S as a function of x in the $Co_xMn_{4-x}N$ films. The M_S values of the $Co_xMn_{4-x}N$ films are summarized in Table I. In going to larger x, M_S first decreases and takes its minimum at $x = 0.8$ and then increases and saturates. This result is rather unexpected, because a monotonic increase is generally expected for a simple evolution from ferrimagnetic Mn_4N to ferromagnetic Co_4N. It also tells us that one can control not only magnetic anisotropy but also M_S in a wide range from 15 to 1350 emu/cm³ by precisely tuning Co concentration in the films.

To unravel the observed M_S behavior, the element-specific magnetic properties of the $Co_xMn_{4-x}N$ films has been studied through XMCD measurements for the Co and Mn $L_{2,3}$ edges. Figures 5(a) and 5(b) show the element-specific hysteresis loops for Mn in the Mn_4N film and for Co and Mn in the $Co_{0.8}Mn_{3.2}N$ film, respectively. The photon energies were fixed at those in which the XMCD amplitude of Co L_3 or Mn L_3 edge is maximized [see Figs. 5(e), 5(j), and 5(k)]. The XMCD intensity is normalized by those at $H = 50$ kOe. A finite value of M_S at 300 K in the $Co_{0.8}Mn_{3.2}N$ film is confirmed. The identical Mn and Co loops for the $Co_{0.8}Mn_{3.2}N$ film indicate a coherent rotation of the Mn and Co 3d moments with the applied field. The hysteresis loop for Mn in the Mn_4N film shows a good squareness, while for the $Co_{0.8}Mn_{3.2}N$ film, the squareness is degraded by the decrease in K_u as described above. We find that the result in Fig. 5(b) is overall consistent with the magnetization in Fig. 4(a) except a nonsaturated behavior of the XMCD amplitude. It can be speculated that such a discrepancy comes from the contribution of paramagnetic interface between the capping layer (~3 nm) and the nitride layer. We note that the probing depth

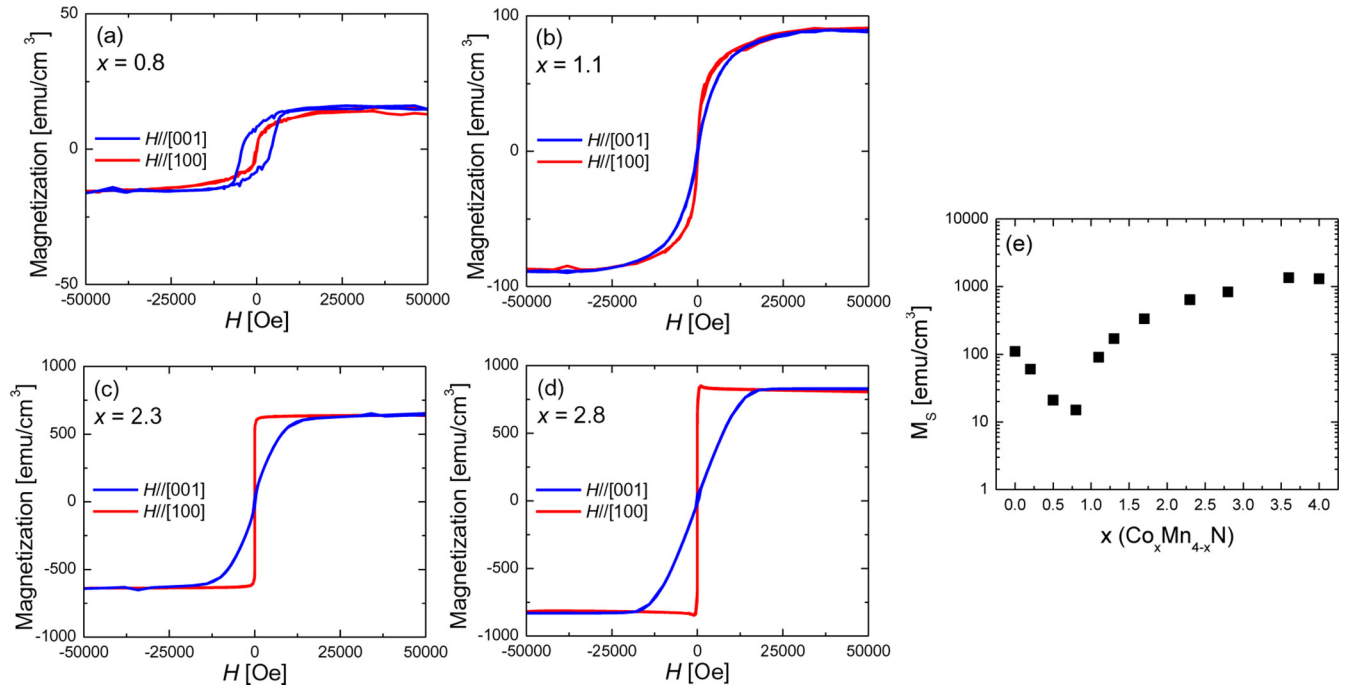FIG. 4. M-H curves of the $Co_xMn_{4-x}N$ [$x =$ (a) 0.8, (b) 1.1, (c) 2.3, and (d) 2.8] films measured at 300 K. H was applied parallel (red) or perpendicular (blue) to the sample surface. (e) x dependence of M_S in the $Co_xMn_{4-x}N$.

of the XMCD measurement using total electron yield method is typically 3–5 nm from the surface [40], which validates the assumption.

We show the Co $L_{2,3}$-edge XAS and XMCD spectra of the $Co_{0.8}Mn_{3.2}N$ film measured at 300 K together with the results from the Co_4N film [32] in Figs. 5(c)–5(f). Since the XAS and XMCD spectra are highly sensitive to the local electronic structure reflecting the local environment [26,41], the difference in spectral shape illustrates that the Co atoms in the $Co_{0.8}Mn_{3.2}N$ film preferentially, not randomly, occupy either the I or II atomic sites in the $Co_xMn_{4-x}N$ lattice. In our previous studies on $Co_xFe_{4-x}N$ and $Ni_xFe_{4-x}N$ films, the transition metals at the I (II) site exhibit localized (itinerant) $3d$ states [26,41]. This is the case for Mn_4N as supported by the FLAPW calculation described below. The line shapes of the XAS [Fig. 5(d)] and XMCD [Fig. 5(f)] spectra of

TABLE I. M_S values of the $Co_xMn_{4-x}N$ films measured at 300 K.

x	M_S [emu/cm^3]
0	110
0.2	60
0.5	21
0.8	15
1.1	90
1.3	170
1.7	335
2.3	640
2.8	830
3.6	1350
4.0	1300

Co_4N are very similar to those of Co metal as reported previously [32]. The broad shoulders on the high-energy side of each main peak in the XAS data are more prominent in $Co_{0.8}Mn_{3.2}N$, which involve the appreciable modifications in the XMCD shape. A detailed analysis is required for a full description of the experimental results to identify the Co-dominated site in the $Co_{0.8}Mn_{3.2}N$ film. Note that the same sign of the XMCD spectra indicates that the Co moment in the $Co_{0.8}Mn_{3.2}N$ film is oriented parallel to the field. Here, we apply the magneto-optical sum rules [42] to the XAS and XMCD spectra of the Co $L_{2,3}$ edges in the $Co_{0.8}Mn_{3.2}N$ film shown in Figs. 5(c) and 5(e), and deduce m_{spin} and the orbital magnetic moment (m_{orb}) per Co atom. The hole number of Co $3d$ states is determined following the method described in Ref. [43]. m_{spin} and m_{orb} obtained are 0.035 ± 0.002 and $0.0036 \pm 0.0002 \, \mu_B/Co$ atom, respectively, to yield a ratio of $m_{orb}/m_{spin} = 0.10$. This ratio coincides with that for the Co_4N film within the experimental error. The ratio is sometimes, but not always, a measure of the degree of localization of moments on Co. Thus again it is difficult to conclusively determine the Co-dominated site in the $Co_{0.8}Mn_{3.2}N$ film. The total moment of $m_{spin} + m_{orb} = 0.038 \mu_B/Co$ is equivalent to approximately $5 \, emu/cm^3$ for the unit cell's volume of the $Co_{0.8}Mn_{3.2}N$ film (58.8 Å^3).

Figures 5(g)–5(l) show the Mn $L_{2,3}$- edge XAS and XMCD spectra of the $Co_{0.8}Mn_{3.2}N$ and Mn_4N films measured at 300 K, together with those from $MnFe_2O_4$. The spectral shapes of $MnFe_2O_4$ are characterized by the final state multiplets of the $2p^53d^6$ configuration from a highly localized $Mn^{2+}(3d^5)$ ground state [44]. Such fine structures emerge as a result of electron localization and are caused by the intra-atomic electrostatic coupling between a created core hole and the $3d$ holes of the outer shell [45]. The multiplet structure
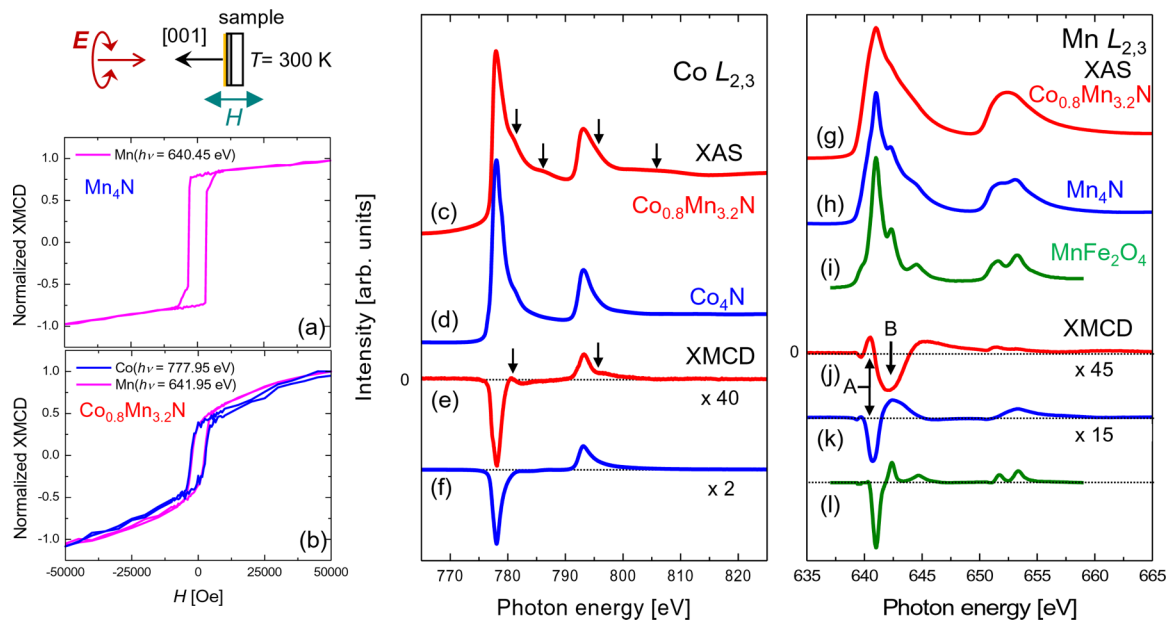
FIG. 5. Element-specific hysteresis loops for (a) Mn atoms of the Mn_4N film, and (b) Co and Mn atoms of the $Co_{0.8}Mn_{3.2}N$ film. (c)–(f) XAS and XMCD spectra at the Co $L_{2,3}$ edges for $Co_{0.8}Mn_{3.2}N$ and Co_4N. (c), (e) and (d), (f) are those for $Co_{0.8}Mn_{3.2}N$ and Mn_4N, respectively. (g)–(l) XAS and XMCD spectra at the Mn $L_{2,3}$ edges for $Co_{0.8}Mn_{3.2}N$, Mn_4N, and $MnFe_2O_4$ [44]. (g), (j), (h), (k), and (i), (l) are those for $Co_{0.8}Mn_{3.2}N$, Mn_4N, and $MnFe_2O_4$, respectively. Measurement was conducted at 300 K with H applied perpendicular to the film surface.

superimposed on a metallic broad shape in the XAS spectra is less pronounced in $Co_{0.8}Mn_{3.2}N$ than in Mn_4N. This strongly suggests that Co atoms in the $Co_{0.8}Mn_{3.2}N$ film preferentially substitute into the I site for Mn with an essentially localized Mn $3d^5$ character [26], while Mn atoms in this film are largely located at the II site with highly metallic character.

The XMCD spectrum of the Mn_4N film in Fig. 5(k) can also be viewed as an overlap of such ionic and metallic components characterized by features A and B, respectively, with opposite signs. This is associated with the ferrimagnetic order, in which the localized Mn(I) (feature A) and metallic Mn(II) (feature B) moments are coupled antiparallel, while the Mn(I) moment aligned parallel to the field. In the $Co_{0.8}Mn_{3.2}N$ film, the XMCD amplitude of B relative to A is enhanced, consistent with the preferential occupation at the I site of Co. Here, we should note that the composition ratio of the Co atoms in $Co_{0.8}Mn_{3.2}N$ is 16 at%, meaning that some Mn atoms are located at the I site even if all the Co atoms occupy the I site. More importantly, the signs of the XMCD signals for A and B are both reversed. Since the Co(I) moment is antiparallel to the Mn(I) moment, this finding indicates that the Mn(I) moment provides a negative contribution to the total magnetization in the $Co_{0.8}Mn_{3.2}N$ film [as schematically shown later in Fig. 8(c)]. We performed the sum-rule analysis to the Mn $L_{2,3}$- edge XAS and XMCD spectra of the $Co_{0.8}Mn_{3.2}N$ film shown in Figs. 5(g) and 5(j) using the method described in Ref. [46] with the $3d$ hole number (n_h) of 5.4 predicted by the first-principles calculation [Fig. 6(a)]. Site-averaged m_{spin} is estimated to be approximately $0.025 \pm 0.003 \, \mu_B$/Mn, and that for m_{orb} falls to zero within the experimental accuracy. This small site-averaged m_{spin} value is consistent with the decrease of the total magnetization with increasing x up to around $x = 1$ shown in Fig. 4(e). This indicates the shrink of $|m_{spin}|$ in Mn(II) by replacing Mn(I) with Co.

To understand the experimental XMCD spectra of Mn_4N in more detail, we have performed FLAPW calculations. We first show the theoretical density of states of Mn_4N in Fig. 6(a). Here we assume the ferrimagnetic spin structure as depicted in Fig. 6(b) because the c/a value of Mn_4N with this spin structure is calculated to be 0.98 [39,47], which is close to the experimental values [10–13]. In Fig. 6(a), narrow and wide bandwidths are obtained for Mn(I) and Mn(II), respectively. This suggests the localized and itinerant feature of the $3d$ electrons in Mn(I) and Mn(II), respectively. The calculated values of m_{spin} for the Mn atoms at I, IIB, and IIA inequivalent sites, and N atoms are 3.07, 0.64, -2.29, and 0.07 μ_B/atom, respectively, as schematically shown in Fig. 6(b). These calculated m_{spin} values are close to those reported in Refs. [39,47]. Total m_{spin} is calculated to be $-0.80 \mu_B$/f.u. This value corresponds to a M_S of 131 emu/cm^3, similar to that found experimentally ($=110$ emu/cm^3) for our Mn_4N film shown in Fig. 4(e). For this theoretical magnetic structure, however, the Mn(I) moment is aligned antiparallel to the field, in contrast to what is observed in the XMCD data. This reveals some quantitative discrepancies in the theoretical values. The sign of calculated m_{spin} in the IIA and IIB site is different, which also contrasts with those obtained in Ref. [14]. Figures 7(a)–7(c) show a comparison of the experimental and calculated Mn $L_{2,3}$ XAS and XMCD spectra. The calculated spectra are broadened by Lorentzian functions with full width at half maximum values of 0.97 and 0.36 eV for the L_2 and L_3 edges, respectively [48]. Note that the sign of the theoretical XMCD in Figs. 7(c) and 7(e) is inverted for comparison purpose. The site-resolved spectra shown in Figs. 7(d) and 7(e) help to identify the sources of the theoretical spectral features. The largest negative (positive) XMCD signal at the L_3 (L_2) edge is mainly contributed by Mn(I) followed by some structures from Mn(IIA) as labeled in Fig. 7(c). Although there are
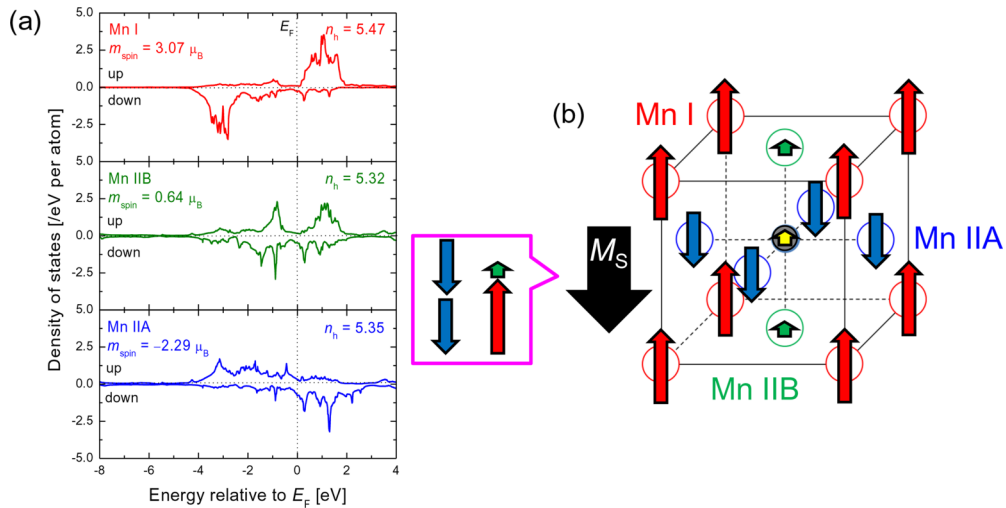
FIG. 6. (a) Total density of states of each Mn site in Mn_4N calculated by the first-principles calculation, and (b) its ferrimagnetic spin structure with direction and magnitude of m_{spin} (red, blue, green, and yellow arrows) and M_S (black arrow).

some discrepancies, the theoretical XMCD curve captures the important qualitative features in the experimental L_3- edge XMCD spectrum. This likely supports our interpretation of the XMCD data that features A and B originate from Mn(I) and Mn(II), respectively. In addition, this comparison indicates that our theoretical treatment is oversimplified [49] and the need for a more advanced theoretical modeling with the core hole-$3d$ and $3d$-$3d$ interactions even in this metallic Mn_4N. In this paper, we do not aim to get a perfect agreement between the experimental and calculated results. We rather intend to place an emphasis on understanding the occupation sites and the spin orientations of the introduced Co atoms. The current calculated spectrum reproduces the experimental spectrum qualitatively and is considered to be sufficient to discuss the evolution of spin structure of $Co_xMn_{4-x}N$.

As shown below in (I)–(V), we summarize the main points in the interpretation of magnetic properties of $Co_xMn_{4-x}N$. (I) M_S takes the minimum around $x = 0.8$ [Fig. 4(e)]. (II) Since the line shapes of the XAS spectrum of $Co_{0.8}Mn_{3.2}N$ shown in Fig. 5(c) and that of Co_4N in Fig. 5(d) are different, Co atoms in $Co_{0.8}Mn_{3.2}N$ are located in a specific site unlike Co_4N. (III) The sign of the XMCD spectrum shown in Fig. 5(e) indicates

that the Co moment in the $Co_{0.8}Mn_{3.2}N$ film is oriented parallel to the total M_S. (IV) The metallic broad shape in the Mn $L_{2,3}$ XAS spectra is more pronounced in $Co_{0.8}Mn_{3.2}N$ [Fig. 5(g)] than in Mn_4N [Fig. 5(h)]. This strongly suggests that Mn atom in the $Co_{0.8}Mn_{3.2}N$ film is preferentially located at the II site with highly metallic character, while Co is located at the I site with an essentially localized character. (V) From the XMCD spectrum of Mn $L_{2,3}$ in $Co_{0.8}Mn_{3.2}N$ [Fig. 5(j)], m_{spin} of itinerant Mn(II) $3d$ electrons (indicated by the sign of peak B) and total M_S direction are parallel to each other. In contrast, m_{spin} of localized Mn(I) $3d$ electrons (indicated by peak A) is antiparallel to M_S. By taking into account (I)–(V), the variation of M_S shown in Fig. 4(e) can be described on the basis of the present XMCD results as shown in Fig. 8. Figures 8(a)–8(c) show schematics of spin structures and M_S for $x = 0, 0.125$, and 0.875 in $Co_xMn_{4-x}N$, respectively, ideally expected from our experiments. In contrast to the theoretical results, $|m_{spin}|$ of Mn(I) surpasses $3 \times |m_{spin}|$ of Mn(II) in ferrimagnetic Mn_4N, which results in uncompensated and small M_S. The total m_{spin} of the I site starts to shrink by substituting Co atoms with the antiparallel magnetic moments and an almost-complete compensation of magnetic moments
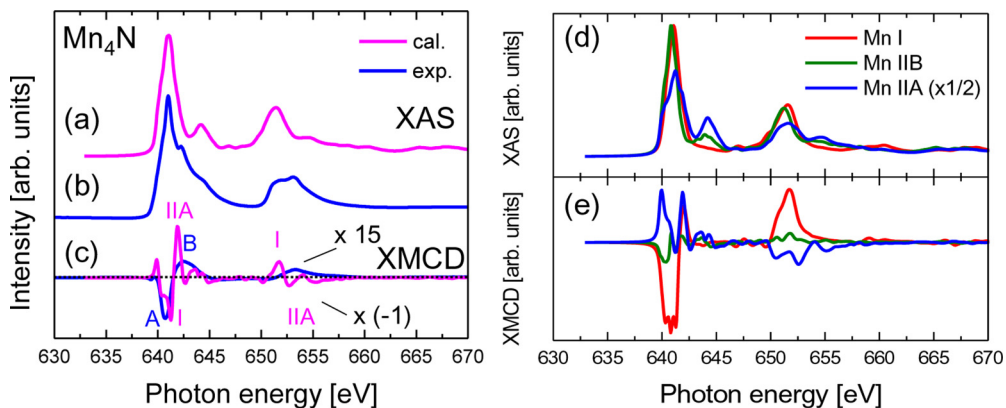

FIG. 7. (a)–(c) Total XAS and XMCD spectra, and (d), (e) partial XAS and XMCD spectra at the Mn $L_{2,3}$ edges of Mn_4N.
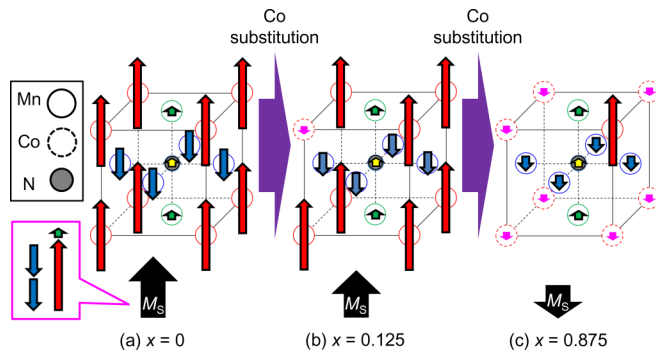
FIG. 8. Schematic of ferrimagnetic spin structure with direction and magnitude of $m_{\rm spin}$ (red, blue, green, and yellow arrows) and M_S (black arrow) for $Co_xMn_{4-x}N$ [x = (a) 0, (b) 0.125, and (c) 0.875] predicted from our experiments.

takes place around a specific Co composition of $x = 0.8$. Above this concentration, the sum of $m_{\rm spin}$ from Co I and Mn II sites further grows together, which explains why M_S increases with x [see Fig. 4(e)].

Finally, we note again that the perpendicular magnetization of $Co_xMn_{4-x}N$ disappears around $x = 1.0$, which corresponds to the case that all Mn(I) atoms are replaced by Co atoms. This implies that the origin of PMA in $Co_xMn_{4-x}N$ is closely related to the difference between the local electronic structure of the Mn(I) and Co(I) atoms under the tetragonal lattice formation of $c/a \sim 0.99$. Further theoretical investigation is required towards a full understanding of the origin of PMA in this system.

IV. CONCLUSION

We grew c-axis-oriented $Co_xMn_{4-x}N$ epitaxial films capped with an Al or a Au layer on STO(001) substrates by MBE. The c/a ratios in the $Co_xMn_{4-x}N$ films were found to be approximately 0.98–0.99 from the XRD measurements for all the samples regardless of x values. The perpendicu-

lar magnetization was clearly observed at 300 K in the M-H curves for $x \leqslant 0.8$, whereas it disappeared for $x \geqslant 1.1$. M_S decreased with increasing x and reached a minimum of $15\,{\rm emu/cm^3}$ at $x = 0.8$ and increased for $0.8 \leqslant x \leqslant 3.6$. We performed XAS and XMCD measurements for the Co and/or Mn $L_{2,3}$ edges of the Co_4N, Mn_4N, and $Co_{0.8}Mn_{3.2}N$ films. We reveal that Co atoms tend to occupy the I site in the $Co_xMn_{4-x}N$ lattice, and their site-averaged $m_{\rm spin}$ and $m_{\rm orb}$ are determined to be 0.035 ± 0.002 and $0.0036 \pm 0.0002\,\mu_{\rm B}/Co$ atom, respectively. More importantly, $m_{\rm spin}$ of the Mn I site is compensated with the sum of Mn II and Co I sites near $x = 0.8$. The line shape of XAS and XMCD spectra for the Mn $L_{2,3}$ edges of Mn_4N is qualitatively described by the calculated spectra. Comparison between experimental and the theoretical spectra reveals the localized and delocalized Mn $3d$ characters at the I and IIA sites. Our findings imply a possibility to manipulate both magnetic anisotropy and M_S by changing x in $Co_xMn_{4-x}N$ films and paves the way to future spintronic devices. Especially, the nearly compensated ferrimagnetic $Co_{0.8}Mn_{3.2}N$ film is suitable for application to current-induced domain-wall motion devices.

[1] S. Ikeda, J. Hayakawa, Y. M. Lee, F. Matsukura, Y. Ohno, T. Hanyu, and H. Ohno, IEEE Trans. Electron Devices **54**, 991 (2007).

[2] S. S. P. Parkin, M. Hayashi, and L. Thomas, Science **320**, 190 (2008).

[3] B. Schulz and K. Baberschke, Phys. Rev. B **50**, 13467 (1994).

[4] R. Thamankar, A. Ostroukhova, and F. O. Schumann, Phys. Rev. B **66**, 134414 (2002).

[5] A. Manchon, C. Ducruet, L. Lombard, S. Auffret, B. Rodmacq, B. Dieny, S. Pizzini, J. Vogel, V. Uhlíř, M. Hochstrasser, and G. Panaccione, J. Appl. Phys. **104**, 043914 (2008).

[6] S. Ikeda, K. Miura, H. Yamamoto, K. Mizunuma, H. D. Gan, M. Endo, S. Kanai, J. Hayakawa, F. Matsukura, and H. Ohno, Nat. Mater. **9**, 721 (2010).

[7] H. Yanagihara, K. Uwabo, M. Minagawa, E. Kita, and N. Hirota, J. Appl. Phys. **109**, 07C122 (2011).

[8] K. M. Ching, W. D Chang, and T. S. Chin, J. Alloys. Compd. **222**, 184 (1995).

[9] K. M. Ching, W. D. Chang, T. S. Chin, J. G. Duh, and H. C. Ku, J. Appl. Phys. **76**, 6582 (1994).

[10] M. Tsunoda and K. Kabara, *presented at International Conference of the Asian Union of Magnetics Societies (ICAUMS) 2012*, 2pPS-47, Nara, Japan, 2012.

[11] Y. Yasutomi, K. Ito, T. Sanai, K. Toko, and T. Suemasu, J. Appl. Phys. **115**, 17A935 (2014).

[12] X. Shen, A. Chikamatsu, K. Shigematsu, Y. Hirose, T. Fukumura, and T. Hasegawa, Appl. Phys. Lett. **105**, 072410 (2014).

[13] K. Kabara and M. Tsunoda, J. Appl. Phys. **117**, 17B512 (2015).

[14] W. J. Takei, R. R. Heikes, and G. Shirane, Phys. Rev. **125**, 1893 (1962).

[15] T. Gushi, M. Klug, J. P. Garcia, S. Ghosh, J. P. Attané, H. Okuno, O. Fruchar, J. Vogel, T. Suemasu, S. Pizzini, and L. Vila, Nano Lett. **19**, 8716 (2019).

[16] S. Kokado, N. Fujima, K. Harigaya, H. Shimizu, and A. Sakuma, Phys. Rev. B **73**, 172410 (2006).

[17] Y. Imai, Y. Takahashi, and T. Kumagai, J. Magn. Magn. Mater. **322**, 2665 (2010).

[18] Y. Takahashi, Y. Imai, and T. Kumagai, J. Magn. Magn. Mater. **323**, 2941 (2011).

[19] I. Pop, R. Muntean, and O. Pop, Mater. Lett. **28**, 155 (1996).

[20] T. Komori, T. Gushi, A. Anzai, L. Vila, J. P. Attané, S. Pizzini, J. Vogel, S. Isogami, K. Toko, and T. Suemasu, J. Appl. Phys. **125**, 213902 (2019).

[21] M. S. Patwari and R. H. Victora, Phys. Rev. B **64**, 214417 (2001).

[22] F. Li, J. Yang, D. Xue, and R. Zhou, Appl. Phys. Lett. **66**, 2343 (1995).

[23] R. Loloee, J. Appl. Phys. **112**, 023902 (2012).

[24] P. Monachesi, T. Björkman, T. Gasche, and O. Eriksson, Phys. Rev. B **88**, 054420 (2013).

[25] F. Takata, K. Kabara, K. Ito, M. Tsunoda, and T. Suemasu, J. Appl. Phys. **121**, 023903 (2017).

[26] F. Takata, K. Ito, Y. Takeda, Y. Saitoh, K. Takanashi, A. Kimura, and T. Suemasu, Phys. Rev. Mater. **2**, 024407 (2018).

[27] A. Anzai, T. Gushi, T. Komori, S. Honda, S. Isogami, and T. Suemasu, J. Appl. Phys. **124**, 123905 (2018).

[28] K. Ito, G. H. Lee, H. Akinaga, and T. Suemasu, J. Cryst. Growth **322**, 63 (2011).

[29] K. Ito, K. Harada, K. Toko, H. Akinaga, and T. Suemasu, J. Cryst. Growh **336**, 40 (2011).

[30] T. Sanai, K. Ito, K. Toko, and T. Suemasu, J. Cryst. Growth **357**, 53 (2012).

[31] K. Ito, G. H. Lee, K. Harada, M. Suzuno, T. Suemasu, Y. Takeda, Y. Saitoh, M. Ye, A. Kimura, and H. Akinaga, Appl. Phys. Lett. **98**, 102507 (2011).

[32] K. Ito, K. Harada, K. Toko, M. Ye, A. Kimura, Y. Takeda, Y. Saitoh, H. Akinaga, and T. Suemasu, Appl. Phys. Lett. **99**, 252501 (2011).

[33] K. Ito, T. Sanai, S. Zhu, Y. Yasutomi, K. Toko, S. Honda, S. Ueda, Y. Takeda, Y. Saitoh, Y. Imai, A. Kimura, and T. Suemasu, Appl. Phys. Lett. **103**, 232403 (2013).

[34] K. Ito, K. Okamoto, K. Harada, T. Sanai, K. Toko, S. Ueda, Y. Imai, T. Okuda, K. Miyamoto, A. Kimura, and T. Suemasu, J. Appl. Phys. **112**, 013911 (2012).

[35] K. Ito, K. Kabara, T. Sanai, K. Toko, Y. Imai, M. Tsunoda, and T. Suemasu, J. Appl. Phys. **116**, 053912 (2014).

[36] K. Oda, T. Yoshio, and K. Oda, J. Mater. Sci. **22**, 2729 (1987).

[37] Y. Saitoh, Y. Fukuda, Y. Takeda, H. Yamagami, S. Takahashi, Y. Asano, T. Hara, K. Shirasawa, M. Takeuchi, T. Tanaka, and H. Kitamura, J. Synchrotron Radiat. **19**, 388 (2012).

[38] T. Ueda, M. Kodera, K. Yamauchi, and T. Oguchi, J. Phys. Soc. Jpn. **82**, 094718 (2013), and references therein.

[39] K. Ito, Y. Yasutomi, K. Kabara, T. Gushi, S. Higashikozono, K. Toko, M. Tsunoda, and T. Suemasu, AIP Adv. **6**, 056201 (2016).

[40] G. van der Laan and A. I. Figueroa, Coord. Chem. Rev. **277-278**, 95 (2014).

[41] K. Ito, K. Toko, Y. Takeda, Y. Saitoh, T. Oguchi, T. Suemasu, and A. Kimura, J. Appl. Phys. **117**, 183906 (2015).

[42] C. T. Chen, Y. U. Idzerda, H. J. Lin, N. V. Smith, G. Meigs, E. Chaban, G. H. Ho, E. Pellegrin, and F. Sette, Phys. Rev. Lett. **75**, 152 (1995).

[43] Y. Takagi, K. Isami, I. Yamamoto, T. Nakagawa, and T. Yokoyama, Phys. Rev. B **81**, 035422 (2010).

[44] J.-S. Kang, G. Kim, H. J. Lee, D. H. Kim, H. S. Kim, J. H. Shim, S. Lee, H. G. Lee, J.-Y. Kim, B. H. Kim, and B. I. Min, Phys. Rev. B **77**, 035121 (2008).

[45] G. van der Laan and B. T. Thole, Phys. Rev. B **43**, 13401 (1991).

[46] K. Nagai, H. Fujiwara, H. Aratani, S. Fujioka, H. Yomosa, Y. Nakatani, T. Kiss, A. Sekiyama, F. Kuroda, H. Fujii, T. Oguchi, A. Tanaka, J. Miyawaki, Y. Harada, Y. Takeda, Y. Saitoh, S. Suga, and R. Y. Umetsu, Phys. Rev. B **97**, 035143 (2018).

[47] S. Isogami, K. Masuda, and Y. Miura, Phys. Rev. Materials **4**, 014406 (2020).

[48] J. L. Campbell and T. Papp, At. Data Nucl. Data Tables **77**, 1 (2001).

[49] J. Lüder, J. Schött, B. Brena, M. W. Haverkort, P. Thunström, O. Eriksson, B. Sanyal, I. Di Marco, and Y. O. Kvashnin, Phys. Rev. B **96**, 245131 (2017).